



## PAPER

[View Article Online](#)  
[View Journal](#) | [View Issue](#)Cite this: *Catal. Sci. Technol.*, 2025, 15, 2852

# Activity enhancement of Ru/TiO<sub>2</sub> catalysts for catalytic hydrogenation of amides to amines through controlling strong metal–support interactions†

Shilong Zhao,<sup>a</sup>  Huaijun Ma,<sup>a</sup> Wei Qu<sup>a</sup> and Zhijian Tian \*<sup>ac</sup>

Efficient and selective catalytic hydrogenation of amides to amines is highly significant but extremely challenging. Here, a series of Ru/TiO<sub>2</sub> catalysts were prepared with the impregnation method at different calcination and reduction temperatures. Multiple characterization tools were used to characterize the physicochemical properties of the catalysts. The hydrogenation of butyramide to butylamine as a model reaction was used to evaluate the catalytic performance. The catalytic activity of the Ru catalyst supported on rutile TiO<sub>2</sub> was superior to that on anatase TiO<sub>2</sub>. As the calcination temperature increased from 200 °C to 600 °C, the catalytic performance of Ru/rutile catalysts monotonously decreased. With the reduction temperature increasing from 200 °C to 600 °C, Ru/rutile catalysts displayed a volcano-like trend of catalytic activity. The Ru/rutile catalyst calcined at 200 °C and reduced at 500 °C exhibited the highest catalytic performance, with 93% butyramide conversion and 65% selectivity to butylamine at 150 °C with 5 MPa H<sub>2</sub>. The evaluation and characterization results suggested that the lattice match between RuO<sub>2</sub> and rutile TiO<sub>2</sub> prevented Ru particle aggregation under high-temperature calcination, and smaller Ru particles were in favor of the amide hydrogenation reaction. The coverage of the TiO<sub>x</sub> overlayer on Ru nanoparticles and the Ru–TiO<sub>x</sub> boundary perimeter were effectively modulated by the strong metal–support interaction under different catalyst reduction temperatures, resulting in the optimization of the amide hydrogenation reactivity over Ru/rutile catalysts. This study facilitates the understanding of the influence of strong metal–support interaction on the catalytic hydrogenation of amide.

Received 20th January 2025,  
Accepted 3rd March 2025

DOI: 10.1039/d5cy00073d

[rsc.li/catalysis](http://rsc.li/catalysis)

## 1. Introduction

Catalytic hydrogenation of amides to amines by using molecular hydrogen is one of the most important and attractive methods among the amine synthesis methods because of its atom-efficient and environmentally benign processes.<sup>1,2</sup> Recently, great efforts have been made to develop efficient heterogeneous catalyst systems for the hydrogenation of various amides.<sup>3–6</sup> Supported catalysts composed of noble metals and reducible metal oxides are usually employed in this reaction and exhibit good catalytic performance, such as Pd–ReO<sub>x</sub>/graphite,<sup>7</sup> Pt–ReO<sub>x</sub>/TiO<sub>2</sub>,<sup>8</sup> Rh–MoO<sub>x</sub>/SiO<sub>2</sub>,<sup>9</sup> Pt–VO<sub>x</sub>/HAP,<sup>10</sup> Ir–MoO<sub>x</sub>/KIT-6,<sup>11</sup> Ru–WO<sub>x</sub>/MgAlO<sub>x</sub>,<sup>12</sup> Rh–VO<sub>x</sub>/Al<sub>2</sub>O<sub>3</sub>,<sup>13</sup> Ru–WO<sub>x</sub>/

SiO<sub>2</sub>,<sup>14</sup> Ru–MoO<sub>x</sub>/SiO<sub>2</sub>,<sup>15</sup> Ru–MoO<sub>x</sub>/TiO<sub>2</sub>,<sup>16</sup> Pt–MoO<sub>x</sub>/TiO<sub>2</sub>,<sup>17,18</sup> Pt/Nb<sub>2</sub>O<sub>5</sub>,<sup>18</sup> Re/TiO<sub>2</sub>,<sup>19</sup> and Ru/Nb<sub>2</sub>O<sub>5</sub>.<sup>20</sup> These catalysts can be categorized into two types. One type encompasses catalysts supported on non-reducible supports like SiO<sub>2</sub> and Al<sub>2</sub>O<sub>3</sub>, and the addition of reducible metal oxides as promoters is necessary to regulate the catalytic performance. The supports merely play a role in dispersing the noble metal components. The other type comprises catalysts supported on reducible supports like TiO<sub>2</sub> and Nb<sub>2</sub>O<sub>5</sub>. Such reducible supports not only disperse the noble metals components but also exert the role of promoters.

Reducible supports have garnered significant attention in recent years due to their positive and diversified effects in many catalyst systems.<sup>21,22</sup> As a reducible metal oxide, TiO<sub>2</sub> is considered to be a superior support in many hydrogenation reactions due to its various crystal phases and abundant interactions with supported noble metals.<sup>23,24</sup> Ru has been demonstrated to be a type of promising noble metal because of its high catalytic hydrogenation activity, unique interaction with TiO<sub>2</sub>, and much lower price in comparison with Pt, Pd, and Rh.<sup>25–27</sup>

<sup>a</sup> Dalian Institute of Chemical Physics, Chinese Academy of Sciences, Dalian, 116023, China. E-mail: [tianz@dicp.ac.cn](mailto:tianz@dicp.ac.cn)

<sup>b</sup> University of Chinese Academy of Sciences, Beijing 100049, China

<sup>c</sup> State Key Laboratory of Catalysis, Dalian Institute of Chemical Physics, Chinese Academy of Sciences, Dalian, 116023, China

† Electronic supplementary information (ESI) available. See DOI: <https://doi.org/10.1039/d5cy00073d>

Much research has reported the distinctive catalytic performance over different crystal phase TiO<sub>2</sub>-supported Ru catalysts across various reactions. Hernandez-Mejia *et al.* investigated the influence of the TiO<sub>2</sub> crystal structure for Ru/TiO<sub>2</sub>-catalysed hydrogenation of xylose. The better dispersed Ru particles over rutile TiO<sub>2</sub> than that on anatase TiO<sub>2</sub> was attributed to a good lattice match between RuO<sub>2</sub> and rutile TiO<sub>2</sub>.<sup>28</sup> Li *et al.* reported that CO<sub>2</sub> hydrogenation selectivity could be tuned by changing the crystal phase of TiO<sub>2</sub>-supported Ru catalysts. The more charge transferred from Ru particles to anatase TiO<sub>2</sub> in comparison with rutile TiO<sub>2</sub> and electron-deficient Ru weakened the adsorption and subsequent activation of the CO intermediate, resulting in high selectivity to CO.<sup>29</sup> Omotoso *et al.* discovered that the stability of Ru particles on Ru/TiO<sub>2</sub> catalysts depended on the TiO<sub>2</sub> crystal phases in the guaiacol hydrodeoxygenation reaction and Ru particles were stabilized by rutile TiO<sub>2</sub> during calcination regeneration.<sup>30</sup> Zhang *et al.* reported that Ru particles supported on different TiO<sub>2</sub> crystal phases resulted in different reaction pathways for the hydrogenation of 4-nitroacetophenone. Since the distance of adjacent Ti atoms of the rutile TiO<sub>2</sub> surface is closer to the N=N bond length of the hydroxylamine intermediate compared with that of the anatase TiO<sub>2</sub> surface, the hydroxylamine species adsorbed on rutile TiO<sub>2</sub> are more susceptible to the coupling reaction.<sup>31</sup> In summary, a suitable crystal phase TiO<sub>2</sub> support can be used to adjust the dispersion of metal nanoparticles, improve the stability of catalysts, and even impact the reaction pathways, thereby enabling the supported catalysts to display distinctive catalytic performance.

In addition, Ru particles supported on TiO<sub>2</sub> undergo dynamic reconstruction of geometric and electronic structure due to the metal-support interaction (MSI) under high-temperature calcination and reduction.<sup>32–34</sup> These dynamic MSIs strongly alter the adsorption properties and active sites in heterogeneous catalysis, widely affecting or even dominating the catalytic hydrogenation performance. Xu *et al.* found that the activity of Ru/TiO<sub>2</sub> catalysts in CO<sub>2</sub> methanation depended on the encapsulation extent of Ru particles by TiO<sub>x</sub> overlayers.<sup>35</sup> Tu *et al.* discovered that the charge transferred from TiO<sub>2</sub> to Ru particles over the Ru/TiO<sub>2</sub> catalyst after high-temperature reduction and electron-rich Ru species facilitated the hydrogenation or desorption steps of olefin intermediates, avoiding the combined C–C cracking to produce methane and favoring more liquid fuels in selective hydrogenolysis of polyolefins.<sup>36</sup> Zhang *et al.* reported that high-temperature calcination favored the formation of Ru–O–Ti bonding in the Ru<sub>x</sub>Ti<sub>1–x</sub>O<sub>2</sub> interphase, which promoted the formation of migrated TiO<sub>x</sub> overlayer on Ru particles upon H<sub>2</sub> reduction and enhanced the activity of CO<sub>2</sub> methanation.<sup>37</sup> In general, the MSI modes relate to charge transfer, the interfacial perimeter, nanoparticle morphology, chemical composition and strong metal-support interaction (SMSI), and SMSI is a distinct phenomenon within the broader concept of MSI.<sup>38,39</sup> Thus, regulating the interactions between the metal and the support is an effective strategy to

optimize the catalytic hydrogenation performance of amide to amine in heterogeneous catalysis.

Here, we prepared a series of Ru/TiO<sub>2</sub> catalysts (Ru/rutile: rutile TiO<sub>2</sub>-supported Ru catalyst, Ru/anatase: anatase TiO<sub>2</sub>-supported Ru catalyst) and investigated the influence of the TiO<sub>2</sub> crystal phase, catalyst calcination, and reduction temperature on the hydrogenation of amide to amine. An array of characterization tools, such as XRD, TEM, CO chemisorption, H<sub>2</sub>-TPR, NH<sub>3</sub>-TPD, CO-DRIFTS, and XPS, were used to research the physicochemical properties of catalysts. The TiO<sub>2</sub> crystal phases and catalyst calcination temperature adjusted Ru particle sizes over catalysts, and the catalytic amide hydrogenation reaction performance was further optimized by changing the reduction temperature of catalysts to control the SMSI over rutile TiO<sub>2</sub>-supported Ru catalysts. The structure–performance relationship was discussed to identify the active sites in Ru/rutile catalysts for the amide hydrogenation reaction.

## 2. Experimental

### 2.1 Catalyst preparation

TiO<sub>2</sub>-supported Ru catalysts (Ru loading of 4 wt%) were prepared by an impregnation–calcination–reduction method. Typically, 0.96 g TiO<sub>2</sub> powder was added to 0.8 mL RuCl<sub>3</sub> solution (0.05 g<sub>Ru</sub> mL<sup>−1</sup>). After mixing the Ru precursor solutions with TiO<sub>2</sub>, the sample was kept for 12 h at room temperature and dried at 120 °C. Finally, the sample was calcined at *X* °C under an air flow for 5 h and was reduced at *Y* °C under a H<sub>2</sub> flow for 2 h. The catalyst is denoted as Ru/TiR-XC-Y or Ru/TiA-XC-Y (R represents the rutile TiO<sub>2</sub>, and A represents the anatase TiO<sub>2</sub>. *X* represents the catalyst calcination temperature, with 200–600 °C, and *Y* represents the catalyst reduction temperature, with 200–600 °C). As a distinction, the unreduced sample is called Ru/TiR-XC or Ru/TiA-XC.

### 2.2 Catalyst characterization

X-ray diffraction (XRD) analysis of the samples was collected on an Empyrean-100 X-ray diffractometer using nickel-filtered Cu Kα radiation in the 2θ range of 5–90° (λ = 1.5418 Å). The operating voltage and current were 40 kV and 40 mA, respectively.

Transmission electron microscopy (TEM) was carried out on a JEM-2100 transmission electron microscope operating at 200 kV. The Ru particle sizes were determined from TEM images, and 100–250 Ru particles were counted for each sample.

N<sub>2</sub> physisorption was carried out on a Micromeritics ASAP 2040 instrument to measure the surface areas, pore volumes, and sizes of the samples. After pretreating at 350 °C for 8 h under vacuum conditions, the sample adsorbed N<sub>2</sub> at −196 °C.

CO chemisorption experiments were carried out on an AutoChem II 2920 analyzer with a TCD detector. The catalyst (~100 mg) was pretreated *in situ* by flowing 10 vol% H<sub>2</sub>–Ar at 400 °C for 1 h, followed by purging with high-purity He for 1 h. After the catalyst was cooled to 40 °C, pulses of 10 vol%

CO–He were injected at regular intervals until CO adsorption was saturated. The number of Ru particles were calculated from the amount of CO adsorbed by assuming that one Ru atom adsorbs one CO molecule.

Temperature-programmed reduction with H<sub>2</sub> (H<sub>2</sub>-TPR) was carried out on an AutoChem II 2920 instrument with a TCD detector. Before TPR measurement, the sample (~100 mg) was pretreated in high-purity He at 400 °C for 1 h, then cooled to 50 °C. The temperature ramp was set at a linear rate of 10 °C min<sup>-1</sup> from 50 °C to 800 °C under 10 vol% H<sub>2</sub>–Ar flows.

Temperature-programmed desorption of NH<sub>3</sub> (NH<sub>3</sub>-TPD) was measured on an AutoChem II 2920 apparatus with a TCD detector. The catalyst was pretreated in a high-purity He flow for 0.5 h at 350 °C and cooled to 100 °C. After the sample had adsorbed NH<sub>3</sub>, the temperature was increased to 700 °C at a 10 °C min<sup>-1</sup> linear rate to desorb NH<sub>3</sub>.

*In situ* CO diffuse reflectance infrared Fourier-transform (CO-DRIFT) spectra and hydroxyl group IR spectra were obtained on a Thermo Scientific Nicolet iS-50 FTIR spectrometer equipped with a liquid nitrogen-cooled mercury–cadmium–telluride (MCT) detector. For each CO adsorption measurement, the sample was *in situ* reduced with H<sub>2</sub> for 1 h at the appropriate temperature and cooled to 25 °C. The gas flow was switched to high-purity Ar flow and held for 10 min. The background spectrum was collected, which was also as hydroxyl group IR spectrum. Then, CO flow was introduced into the cell until reaching the saturated adsorption of CO and subsequently purged with Ar flow to remove gaseous CO. Finally, the DRIFTS spectrum of CO was recorded from 4000 to 600 cm<sup>-1</sup> for 64 scans at a resolution of 4 cm<sup>-1</sup>.

X-ray photoelectron spectroscopy (XPS) measurement was performed on a VG ESCALAB 250Xi spectrometer with monochromatized Al K $\alpha$  excitation, and the binding energies were calibrated by the C 1s peak at 284.6 eV. After reduction in the tube furnace, the reduced catalysts were sealed inside a glove box and transferred into an XPS vacuum chamber.

### 2.3 Catalytic test

Butyramide, as a model reactant, was used to evaluate the catalytic performance of the Ru/TiO<sub>2</sub> catalysts. Reactions were performed in a 100 mL high-pressure Parr 4848 batch reactor. For a typical test, 300 mg catalyst, 3 mmol butyramide, and 25 mL cyclopentyl methyl ether (CPME) were introduced to the high-pressure Parr batch reactor. Then, the reactor was sealed, purged three times with nitrogen and hydrogen, respectively, and pressurized up to the desired H<sub>2</sub> pressure at room temperature. Finally, the reactor was heated to the desired temperature and an appropriate reaction time under constant stirring at 300 rpm. Upon completion of the reaction, the reactor was quickly cooled to room temperature with ice water. The reactor was opened after the pressure was released. The liquid reaction mixture was filtered and then analyzed by GC-MS on an Agilent 7890B instrument with a

flame ionization detector (FID) and a DB-1 column (50 m  $\times$  0.32 mm  $\times$  0.25  $\mu$ m). The conversion of butyramides was kept below 35% by adjusting the reaction time to measure the intrinsic activity for the reaction order experiments.

The conversion of amide, the selectivity, and the yield of product *i* were calculated using the following formulas:

$$\text{Conversion} = (1 - n_x/n_o) \times 100\% \quad (1)$$

$$\text{Selectivity} = (n_i/n_c) \times 100\% \quad (2)$$

$$\text{Yield} = (n_i/n_o) \times 100\% \quad (3)$$

where  $n_x$  is the residual molar amount of amide after reaction,  $n_o$  is the initial molar amount of amide fed,  $n_i$  is the molar amount of amide converted to product *i*, and  $n_c$  is the total molar amount of amide converted.

## 3. Results and discussion

### 3.1 The influence of the TiO<sub>2</sub> crystalline phase structure on Ru/TiO<sub>2</sub> catalysts

**3.1.1 The catalyst characterization of Ru/TiO<sub>2</sub> catalysts with rutile and anatase TiO<sub>2</sub>.** Taking the catalysts calcined at 350 °C and reduced at 400 °C as examples, the XRD patterns of Ru catalysts supported on rutile and anatase TiO<sub>2</sub> (Ru/TiR-350C-400 and Ru/TiA-350C-400) as well as their unreduced samples (Ru/TiR-350C and Ru/TiA-350C), are presented in Fig. 1. For anatase TiO<sub>2</sub>-supported Ru samples, the XRD peaks at  $2\theta = 25.3^\circ, 36.9^\circ, 37.9^\circ, 38.6^\circ, 48.4^\circ, 53.9^\circ, 55.3^\circ, 62.7^\circ, 69.0^\circ, 70.2^\circ$ , and  $75.4^\circ$  correspond to the characteristic diffraction peaks of anatase TiO<sub>2</sub>.<sup>40</sup> The weak peaks at  $29.0^\circ$  and  $44.2^\circ$  are assigned to the large particle size of RuO<sub>2</sub>,<sup>41</sup> and the weak peak at  $44.0^\circ$  is assigned to metallic Ru.<sup>42</sup> This result indicates that RuO<sub>2</sub> agglomerates on anatase TiO<sub>2</sub> after calcination and forms large Ru particles after reduction.

For rutile TiO<sub>2</sub>-supported Ru samples, the XRD peaks at  $2\theta = 27.5^\circ, 36.0^\circ, 39.3^\circ, 41.2^\circ, 44.1^\circ, 54.2^\circ, 56.8^\circ, 62.3^\circ, 64.2^\circ$ ,

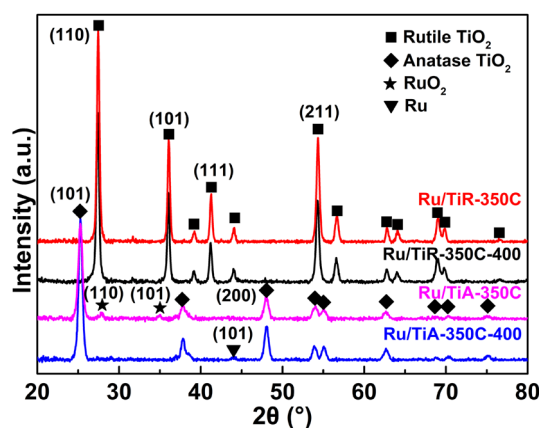


Fig. 1 XRD patterns of rutile and anatase TiO<sub>2</sub>-supported Ru catalysts (Ru/TiR-350C-400 and Ru/TiA-350C-400) and their unreduced samples (Ru/TiR-350C and Ru/TiA-350C).



69.0° and 69.9° correspond to the characteristic diffraction peaks of rutile TiO<sub>2</sub>.<sup>43</sup> However, except for the diffraction peaks of the rutile TiO<sub>2</sub> support, no characteristic peaks of metallic Ru<sup>0</sup> or RuO<sub>2</sub> are observed on the Ru/TiR-350C-400 catalyst and Ru/TiR-350C sample. Considering the Ru loading of 4 wt%, the absence of RuO<sub>2</sub> and Ru<sup>0</sup> peaks is attributed to the high dispersion of Ru species on rutile TiO<sub>2</sub>. The above results indicate a higher dispersion of Ru species on rutile TiO<sub>2</sub>.

Fig. 2(a) presents a TEM image of the Ru/TiR-350C-400 catalyst. Rutile TiO<sub>2</sub> is rod-shaped with a narrow diameter distribution of 30–50 nm and a wide length distribution of 100–120 nm. A large number of Ru particles are highly dispersed on the rutile TiO<sub>2</sub> with a relatively homogeneous distribution. According to the statistical result of the TEM image, the uniform size of Ru particle is ~2 nm. Fig. 2(b) presents a TEM image of the Ru/TiA-350C-400 catalyst. The anatase TiO<sub>2</sub> is spherical with a diameter of ~30 nm. It is observed that the large Ru bulks show a largely inhomogeneous metal distribution. The above results indicate smaller Ru particle sizes on rutile TiO<sub>2</sub>, agreeing with the XRD results.

Table 1 presents the properties of the rutile and anatase TiO<sub>2</sub> and provides the crystal structure parameters of RuO<sub>2</sub> as a comparison. Although rutile TiO<sub>2</sub> provides a smaller BET surface area (25.6 m<sup>2</sup> g<sup>−1</sup>) than anatase TiO<sub>2</sub> (113.0 m<sup>2</sup> g<sup>−1</sup>), Ru particles in rutile TiO<sub>2</sub> have more uniform and narrower size distribution compared with larger Ru bulks in anatase TiO<sub>2</sub>. Wang *et al.* studied the dispersion behaviors of RuO<sub>2</sub> supported on rutile and anatase TiO<sub>2</sub> after high-temperature calcination and discovered that the monolayer dispersion

**Table 1** The properties of RuO<sub>2</sub>, rutile TiO<sub>2</sub>, and anatase TiO<sub>2</sub>

Oxides	Lattice parameters <sup>46</sup>				Textural properties		
	<i>a</i> (Å)	<i>b</i> (Å)	<i>c</i> (Å)	<i>a</i> / <i>b</i> / <i>γ</i> (°)	<i>S</i> <sub>BET</sub> (m <sup>2</sup> g <sup>−1</sup> )	<i>V</i> <sub>pore</sub> (cm <sup>3</sup> g <sup>−1</sup> )	<i>d</i> <sub>pore</sub> (nm)
RuO <sub>2</sub>	4.492	4.492	3.099	90	—	—	—
Rutile TiO <sub>2</sub>	4.594	4.594	2.959	90	25.6	0.17	26.4
Anatase TiO <sub>2</sub>	3.785	3.785	9.512	90	113.0	0.28	10.6

capacity of RuO<sub>2</sub> on rutile TiO<sub>2</sub> was much higher than that on anatase TiO<sub>2</sub>. The lattice match between RuO<sub>2</sub> and rutile TiO<sub>2</sub> forms more abundant Ru–O–Ti interfacial bonds, facilitating RuO<sub>2</sub> dispersion, while fewer Ru–O–Ti interfacial bonds between RuO<sub>2</sub> and anatase TiO<sub>2</sub> resulted in RuO<sub>2</sub> agglomeration.<sup>44</sup> Zhou *et al.* also reported a similar result, that is, the dispersion of Ru particles on rutile and anatase TiO<sub>2</sub> was governed by the lattice match between RuO<sub>2</sub> and TiO<sub>2</sub> crystal phases.<sup>45</sup> Therefore, the good dispersion of Ru particles on rutile TiO<sub>2</sub> is attributed to the lattice match between RuO<sub>2</sub> and rutile TiO<sub>2</sub>, preventing the agglomeration of Ru particles during the calcination step. In contrast, RuO<sub>2</sub> species undergo agglomeration during the calcination process and are reduced to form large Ru bulks since RuO<sub>2</sub> species are unstable and lack such a lattice match with anatase TiO<sub>2</sub>.

**3.1.2 The amide hydrogenation performance of Ru/TiO<sub>2</sub> catalysts with rutile and anatase TiO<sub>2</sub>.** The hydrogenation of butyramide (C<sub>3</sub>H<sub>7</sub>C(O)NH<sub>2</sub>) is used as the model reaction to evaluate the catalytic performance of Ru/TiO<sub>2</sub> catalysts with rutile and anatase TiO<sub>2</sub>. Butylamine (C<sub>4</sub>H<sub>9</sub>NH<sub>2</sub>, –NH<sub>2</sub>) is the target product, and dibutylamine ((C<sub>4</sub>H<sub>9</sub>)<sub>2</sub>N, –NHR), 1-butanol (C<sub>4</sub>H<sub>9</sub>OH, –OH) and *N*-butylbutanamide (C<sub>3</sub>H<sub>7</sub>C(O)NHC<sub>4</sub>H<sub>9</sub>, other) are by-products. The GC-MS spectra of reactants and products are shown in Fig. S1† and the corresponding internal standard curves are shown in Fig. S2.†

Fig. 3 shows the butyramide conversion and product selectivity obtained according to the reaction time using the Ru/TiO<sub>2</sub> catalysts with rutile and anatase TiO<sub>2</sub> in the butyramide hydrogenation reaction. For the Ru/TiR-350C-400 catalyst (Fig. 3(a)), when the reaction time is 1 h, the butyramide conversion is 32% and the selectivity to butylamine, 1-butanol, and dibutylamine is 79%, 19%, and 2%, respectively. As the reaction time is prolonged, the butyramide conversion and the dibutylamine selectivity gradually increase. The butylamine selectivity slightly declines, while the 1-butanol selectivity remains nearly invariant. Additionally, an extremely minute amount of *N*-butylbutanamide is also present in the products. After 12 h of reaction time, the butyramide conversion increases to 87%. The selectivity to butylamine, 1-butanol, dibutylamine, and *N*-butylbutanamide is 63%, 24%, 9% and 4%, respectively. According to the reaction network (Scheme 1), the decreased selectivity to butylamine is caused by the consumption resulting from the secondary side reaction of deamination condensation between

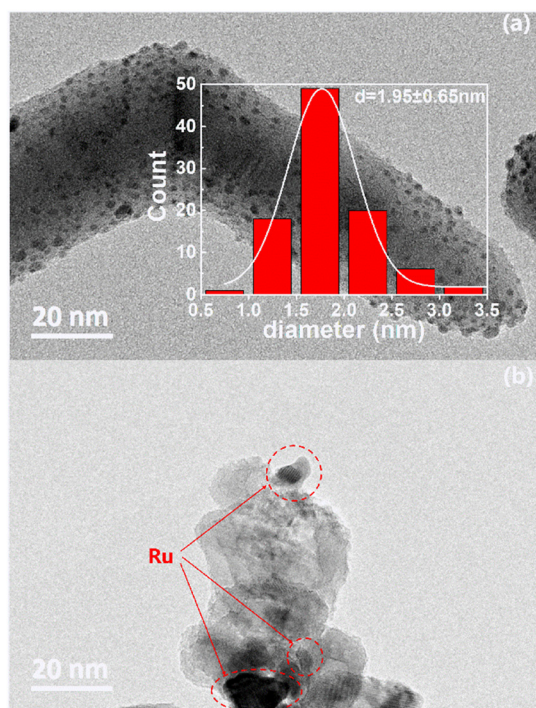


**Fig. 2** TEM images of (a) Ru/TiR-350C-400 and (b) Ru/TiA-350C-400 catalysts.

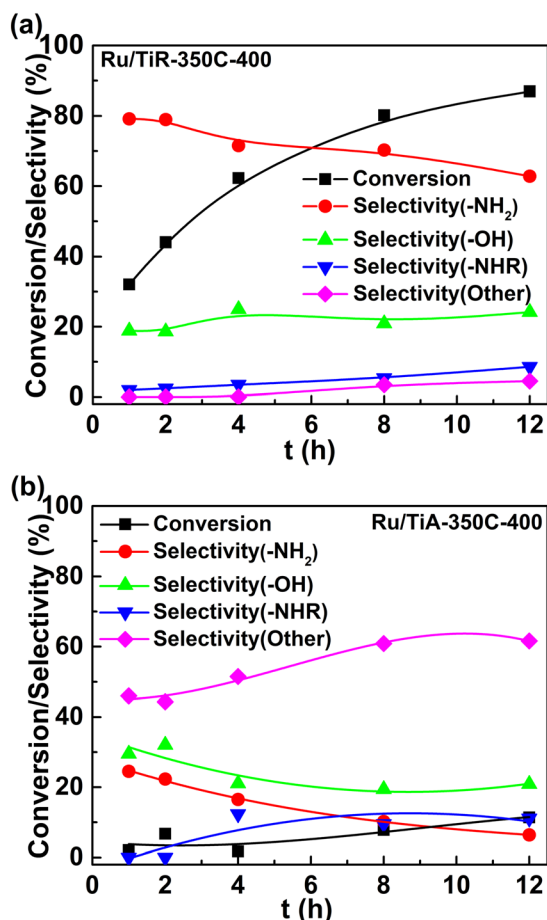


Fig. 3 The catalytic performance of (a) Ru/TiR-350C-400 and (b) Ru/TiA-350C-400 catalysts for butyramide hydrogenation reaction. Reaction conditions: 50 mg catalyst, 3 mmol butyramides, 25 mL CPME, 150 °C, and 5 MPa H<sub>2</sub>.

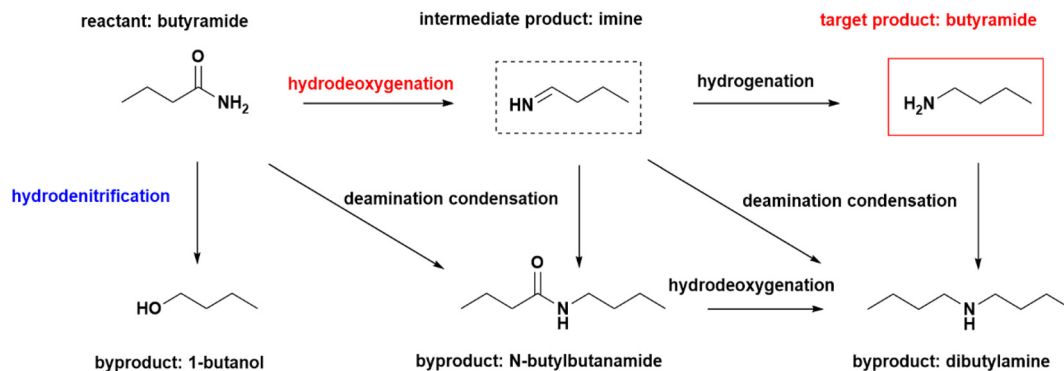
butylamine and imine intermediates. *N*-Butylbutanamide originates from the deamination condensation of butyramide and imine intermediates. The increased selectivity to dibutylamine is not only related to the deamination condensation of butylamine and imine intermediates but also originates from the hydrodeoxygenation of *N*-butylbutanamide.

For the Ru/TiA-350C-400 catalyst (Fig. 3(b)), when the reaction time is 1 h, the butyramide conversion is merely 2%, and the selectivity to butylamine, butanol, and *N*-butylbutanamide is 25%, 29%, and 46%, respectively. Almost no dibutylamine is detected in the product. With the extension of the reaction time, the butyramide conversion increases slowly, and the selectivity to *N*-butylbutanamide and dibutylamine increases to some extent. The selectivity of butylamine decreases slightly, while the selectivity of butanol varies insignificantly. After 12 h, the butyramide conversion increases to 11%. The selectivity to butylamine decreases to 6%, while that to butanol is 21%. The selectivity to *N*-butylbutanamide and dibutylamine increases to 62% and 11%, respectively. Overall, the butyramide hydrodeoxygenation performance over the Ru/TiO<sub>2</sub> catalyst with anatase TiO<sub>2</sub> is unsatisfactory.

Although Ru catalysts supported on rutile and anatase TiO<sub>2</sub> have the same chemical composition, the excellent catalytic performance of the rutile TiO<sub>2</sub>-supported Ru catalyst is in significantly sharp contrast to the poor performance of the anatase TiO<sub>2</sub>-supported Ru catalyst for the butyramide hydrogenation. As shown by TEM images (Fig. 2), small Ru particles disperse on rutile TiO<sub>2</sub>, while large Ru particles disperse on anatase TiO<sub>2</sub>. The MSI between Ru and different crystal phase TiO<sub>2</sub> impacts the Ru particle morphology. Therefore, the higher catalytic performance over the rutile TiO<sub>2</sub>-supported Ru catalyst can be ascribed to the high and uniform dispersion of Ru particles on rutile TiO<sub>2</sub>, providing more active sites for the butyramide hydrogenation reaction. The above results show that rutile TiO<sub>2</sub> appears to be a promising support for the preparation of a highly active Ru catalyst in comparison with anatase TiO<sub>2</sub> and smaller Ru nanoparticles are more in favour of the amide hydrogenation reaction than aminated and larger Ru particles.

### 3.2 The influence of calcination temperature on Ru particle sizes over rutile TiO<sub>2</sub>-supported Ru catalysts (Ru/TiR-XC-500)

**3.2.1 The catalyst characterization of Ru/rutile catalysts with different calcination temperatures.** Fig. 4 presents XRD patterns and partial enlarged details of the rutile TiO<sub>2</sub>-



Scheme 1 The possible reaction network for the hydrogenation of butyramide.

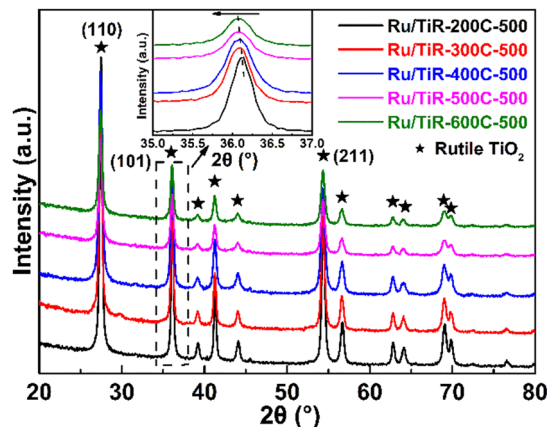


Fig. 4 XRD patterns and partial enlarged details of Ru/rutile catalysts with different calcination temperatures.

supported Ru catalysts calcined at different temperatures and reduced at 500 °C (Ru/TiR-XC-500). The XRD patterns of these catalysts only exhibit the characteristic diffraction peaks of rutile  $\text{TiO}_2$ . The metallic Ru or  $\text{RuO}_2$  phase peaks are not detected, which is attributed to the high dispersion of Ru species. Notably, it is clearly observed that the diffraction peaks of catalysts become weaker with higher calcination temperature, which suggests that the crystallite quality of the rutile  $\text{TiO}_2$  particles deteriorates. In addition, compared with standard rutile  $\text{TiO}_2$  diffraction peaks, the XRD peaks shift slightly towards a lower angle ( $\sim 0.07^\circ$ ) with the higher calcination temperature, which is induced by Ru ion doping in the rutile  $\text{TiO}_2$  nanocrystals due to the ionic radius of the  $\text{Ru}^{4+}$  ion (76 pm) being larger than that of the  $\text{Ti}^{4+}$  ion (64 pm).<sup>47,48</sup> In general, a smaller ionic radius replaced with a larger ionic radius results in the stretching of bond length as well as lattice parameter, which results in the increase of unit cell volume.<sup>49</sup> The above results clearly reveal that Ru particles are highly dispersed on the rutile  $\text{TiO}_2$  support and more Ru ions are doped in the rutile  $\text{TiO}_2$  nanocrystals with the higher calcination temperature of catalysts.

Fig. 5 shows the TEM images of rutile  $\text{TiO}_2$ -supported Ru catalysts calcined at different temperatures and reduced at 500 °C. The rutile  $\text{TiO}_2$  is rod-shaped with a narrow diameter distribution of 30–50 nm and a wide length distribution of 100–120 nm, and the microstructure of rutile  $\text{TiO}_2$  is not affected by high-temperature calcination. The Ru particles are highly dispersed on the rutile  $\text{TiO}_2$  with a relatively homogeneous distribution, and the average Ru particle sizes determined by the TEM images of each catalyst are listed in Table S1.† When the calcination temperature is  $\leq 400$  °C, the Ru particle sizes remain at  $\sim 3$  nm and exhibit no significant change, demonstrating that rutile  $\text{TiO}_2$  can anchor Ru particles well. When the calcination temperature exceeds 400 °C, the Ru particle sizes slightly increase from 3.24 nm to 5.59 nm. Correspondingly, the Ru particle shape also gradually changes from a regular sphere to an ellipsoid, suggesting that the enhanced MSI changes the nanoparticle morphology. The results show that the average sizes of Ru

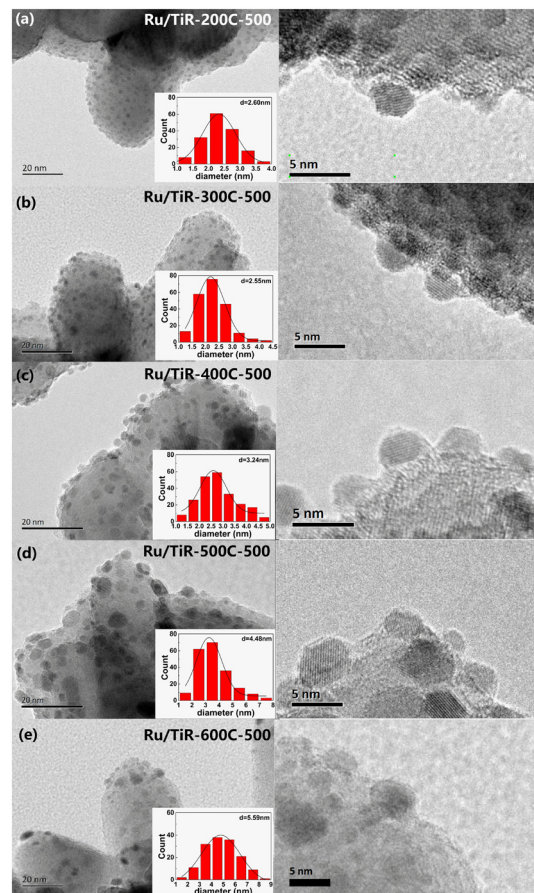


Fig. 5 TEM images of (a) Ru/TiR-200C-500, (b) Ru/TiR-300C-500, (c) Ru/TiR-400C-500, (d) Ru/TiR-500C-500, and (e) Ru/TiR-600C-500 and the particle size distribution of each catalyst.

particles on rutile  $\text{TiO}_2$  gradually enlarge with the catalyst calcination temperature increasing.

$\text{H}_2$ -TPR analysis is performed to study the effects of catalyst calcination temperature on the reducibility of Ru/rutile samples. The  $\text{H}_2$ -TPR profiles are shown in Fig. 6 and the amounts of  $\text{H}_2$  consumption are summarized in Table

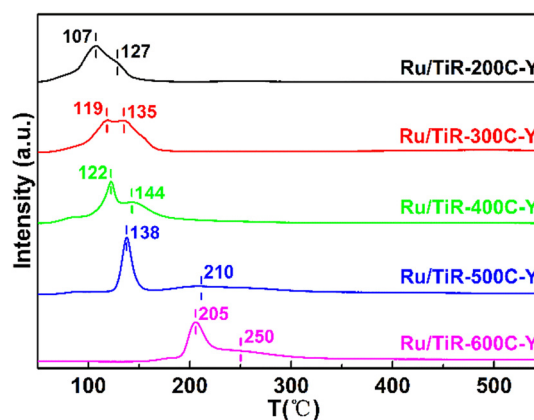


Fig. 6  $\text{H}_2$ -TPR profiles of Ru/rutile samples with different calcination temperatures.



S1† Specifically, the Ru/rutile sample calcined at 200 °C has two main H<sub>2</sub> reduction peaks at 107 °C and 127 °C. It is reported that the reduction temperature of Ru–O–Ti is higher than that of Ru–O–Ru.<sup>50</sup> Thus, the low-temperature peak is ascribed to the reduction of exposed RuO<sub>2</sub> and the high-temperature peak is attributed to the reduction of RuO<sub>2</sub> at the RuO<sub>2</sub>–TiO<sub>x</sub> interface.<sup>51,52</sup> The metallic Ru promotes the reduction of interfacial RuO<sub>2</sub>–TiO<sub>x</sub> via hydrogen spillover from Ru particles to the Ru–TiO<sub>x</sub> boundary during the reduction process.<sup>53</sup> As the catalyst calcination temperature increases from 200 °C to 600 °C, the shapes of the H<sub>2</sub> reduction peaks change and the peak positions shift to higher temperatures. The shape of the low-temperature peak gradually becomes sharper and the peak position shifts to 205 °C, while the shape of the high-temperature peak gradually becomes broader and the peak position shifts to 250 °C. The sharper low-temperature peaks indicate that relatively larger RuO<sub>2</sub> microcrystals are formed in the Ru/rutile samples with the calcination temperature increasing. The broader high-temperature peaks suggest that more Ru–O–Ti species exist in the RuO<sub>2</sub>–TiO<sub>x</sub> interface, following the observation from the XRD results (Fig. 4). In addition, the reduction peaks shifting to higher temperatures may be caused by the gradually enhanced interactions of RuO<sub>2</sub> and rutile TiO<sub>2</sub> with the increase of calcination temperature. More Ru<sup>4+</sup> ions dope in the rutile TiO<sub>2</sub> nanocrystals, making it more difficult to reduce the RuO<sub>2</sub> species.<sup>51,54</sup>

Although the Ru loadings are the same (~4 wt%), the H<sub>2</sub> consumption amounts (Table S1†) for ruthenium oxide species reduction of Ru/rutile samples calcined at different temperatures are diverse from each other and are lower than the theoretical value (0.79 mmol g<sup>-1</sup>) obtained by assuming complete reduction of RuO<sub>2</sub> to Ru. The proportion of reduced Ru species to all Ru species, defined as the reduction degree of ruthenium oxide species (it is calculated based on the ratios of the amount of H<sub>2</sub> consumption to the theoretical H<sub>2</sub> consumption value), is continuously increasing from 0.456 to 0.578 (Table S1†) with the calcination temperature increasing from 200 °C to 600 °C. This result suggests that partial RuO<sub>2</sub> species are not reduced yet. Moreover, combined with the TEM images (Fig. 5) of the Ru/rutile catalysts, the increased reduction degrees are attributed to the larger Ru particle sizes on rutile TiO<sub>2</sub> with the higher catalyst calcination temperature.

The electronic states of Ru species over Ru/rutile catalysts with different calcination temperatures were investigated by XPS analysis, with the peaks illustrated in Fig. 7(a). Since the XPS peaks of C 1s and Ru 3d<sub>3/2</sub> are overlapped with each other, the peak of Ru 3d<sub>5/2</sub> is mainly used for analysis. Specifically, the Ru 3d<sub>5/2</sub> peak of the Ru/TiR-200C-500 catalyst is fitted in two parts which are located at 280.3 eV and 281.3 eV. The former is attributed to Ru<sup>0</sup> and the latter is ascribed to Ru<sup>X+</sup> (0 < X < 4) mainly located at Ru–TiO<sub>x</sub> interfaces.<sup>55,56</sup> It is suggested that the Ru/rutile catalysts still maintain a considerable amount of Ru<sup>X+</sup> species after the reduction, indicating that Ru<sup>X+</sup> originating from the Ru–TiO<sub>x</sub> interfaces

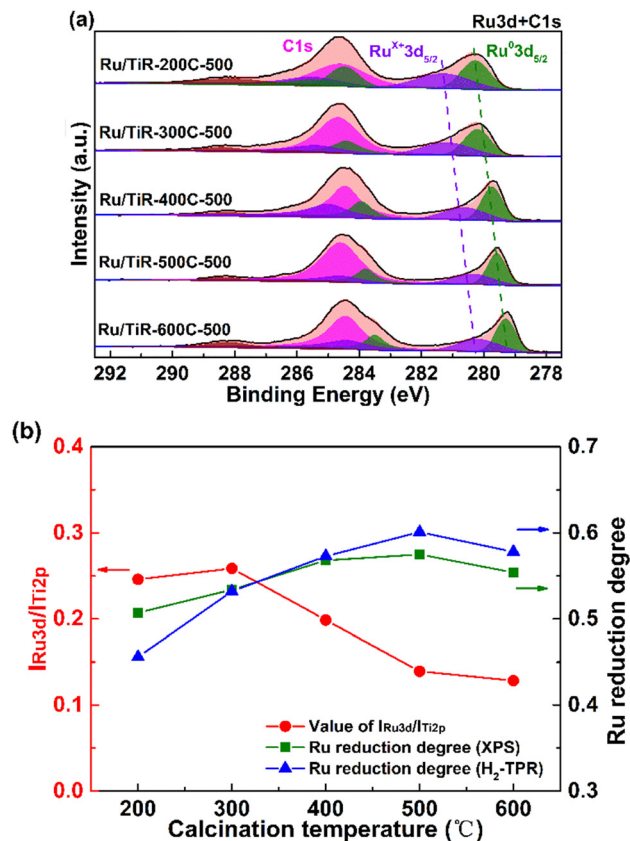


Fig. 7 (a) The XPS fitting results of Ru 3d and (b) the values of  $I_{\text{Ru}3d}/I_{\text{Ti}2p}$  (based on the XPS peak area ratios of Ru 3d and Ti 2p) and Ru reduction degrees (Ru reduction degree (XPS) is calculated based on XPS peak fitting area ratios of Ru 3d, and Ru reduction degree (H<sub>2</sub>-TPR) is calculated based on H<sub>2</sub> consumption of H<sub>2</sub>-TPR) with different calcination temperatures over Ru/rutile catalysts.

is difficult to reduce. As the calcination temperature increases, the binding energies of Ru<sup>0</sup> and Ru<sup>X+</sup> species shift toward lower binding energies. When the calcination temperature increases to 600 °C, the binding energies of Ru<sup>0</sup> and Ru<sup>X+</sup> shift to 279.3 eV and 280.2 eV (Table S2†), respectively. Aiyer *et al.* reported that the variation of the shift in the metal binding energy was correlated with the diameter of the metal nanoparticles.<sup>57</sup> The larger the particle size of a metal was, the closer its binding energy was to the value of the bulk metal. Therefore, the negative shift of the Ru binding energy is attributed to the larger Ru particles with the higher catalyst calcination temperature.

For the supported metal catalysts, it has been shown that the element XPS peak area ratios of metal and support can provide important information about the dispersion of the supported metal particles.<sup>58,59</sup> Fig. 7(b) shows the relationship between the relative content value of  $I_{\text{Ru}3d}/I_{\text{Ti}2p}$  (calculated quantitatively with the XPS peak area ratio of Ru 3d and Ti 2p) and different calcination temperatures over Ru/rutile catalysts. It is noted that the  $I_{\text{Ru}3d}/I_{\text{Ti}2p}$  values monotonously decrease from 0.246 to 0.128 with the calcination temperature increasing from 200 °C to 600 °C

(Table S2 and Fig. S3†), and it demonstrates that the relative signal intensity of Ru species decreased. Considering the same Ru loadings (~4 wt%) in the Ru/rutile catalysts, the decreased  $I_{\text{Ru}3d}/I_{\text{Ti}2p}$  value means worse dispersion of Ru particles calcined at higher temperature. Fig. 7(b) also shows the relationship between Ru reduction degrees and different calcination temperatures over the Ru/rutile catalysts. The Ru reduction degree is quantitatively calculated based on the XPS peak fitting area ratios of Ru 3d ( $\text{Ru}^0/(\text{Ru}^0 + \text{Ru}^{X+})$ ) and the ratios of  $\text{H}_2$  consumption ( $\text{H}_2$ -TPR results) to the theoretical  $\text{H}_2$  consumption value, respectively. It is found that the  $\text{Ru}^0/(\text{Ru}^0 + \text{Ru}^{X+})$  values increase from 0.507 to 0.554 with the calcination temperature increasing (Table S2†), while the Ru reduction degrees by calculating  $\text{H}_2$  consumption increase from 0.456 to 0.578 (Table S1†). The trends of both are similar. In other words, the relative contents of  $\text{Ru}^{X+}$  species decreased with the calcination temperature increasing. The phenomenon is ascribed to the fact that larger Ru particle sizes form less Ru-TiO<sub>x</sub> interface over the Ru/rutile catalysts calcined at higher temperatures.

**3.2.2 The amide hydrogenation performance of Ru/rutile catalysts with different calcination temperatures.** Fig. 8 shows the catalytic performance for the butyramide hydrogenation over the Ru/rutile catalysts calcined at different temperatures. After 4 h of reaction, the butyramide conversion is 93%, and selectivity to butylamine, 1-butanol, dibutylamine, and *N*-butylbutanamide is 65%, 14%, 16%, and 5%, respectively, over the catalyst calcined at 200 °C. As the catalyst calcination temperature increases from 200 °C to 500 °C, it is observed that the butyramide conversion slightly decreases from 93% to 82%, and the selectivity to butylamine, 1-butanol, dibutylamine and *N*-butylbutanamide is not significantly changed. When the calcination temperature is 600 °C, the lowest butyramide conversion (54%) is obtained and selectivity to butylamine, 1-butanol, dibutylamine, and *N*-butylbutanamide is 77%, 14%, 7%, and 2%, respectively. Furthermore, the yield of butylamine gradually decreases from 60% to 42% with the calcination

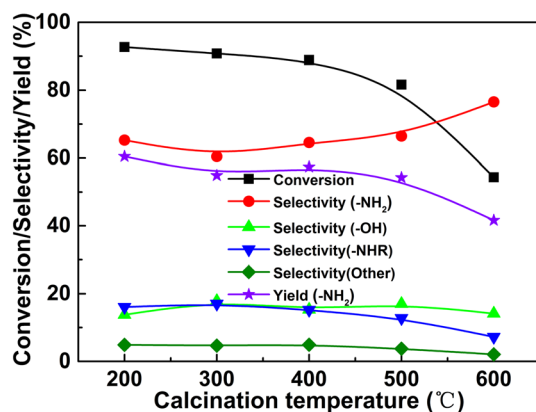


Fig. 8 The catalytic hydrogenation performance of butyramide over Ru/TiR-XC-500 catalysts. Reaction conditions: 300 mg catalyst, 3 mmol butyramides, 25 mL CPME, 150 °C, 5 MPa  $\text{H}_2$ , and 4 h.

temperature increasing. The best catalytic activity and yield of butylamine are obtained over the Ru/rutile catalyst calcined at 200 °C. Combined with the average Ru particle sizes determined by the TEM images of each Ru/rutile catalyst, the catalytic activity of butyramide hydrogenation is correlated with Ru particle size over Ru/rutile, and smaller Ru nanoparticles are more in favour of the amide hydrogenation reaction. In general, smaller sizes of Ru particles mean more exposed metal Ru atoms and more abundant Ru-TiO<sub>x</sub> boundaries. Thus, further investigation is needed to determine which one may be the active site of amide hydrogenation.

### 3.3 The influence of reduction temperature on SMSI over rutile TiO<sub>2</sub>-supported Ru catalysts (Ru/TiR-200C-Y)

**3.3.1 The catalyst characterization of Ru/rutile catalysts with different reduction temperatures.** Fig. 9 shows TEM images of the Ru/rutile catalysts calcined at 200 °C and reduced at different temperatures, and the Ru particle sizes are calculated based on TEM images. The Ru nanoparticles, with particle sizes of 2–3 nm, are highly dispersed on the rutile TiO<sub>2</sub> support for all catalysts, which is consistent with

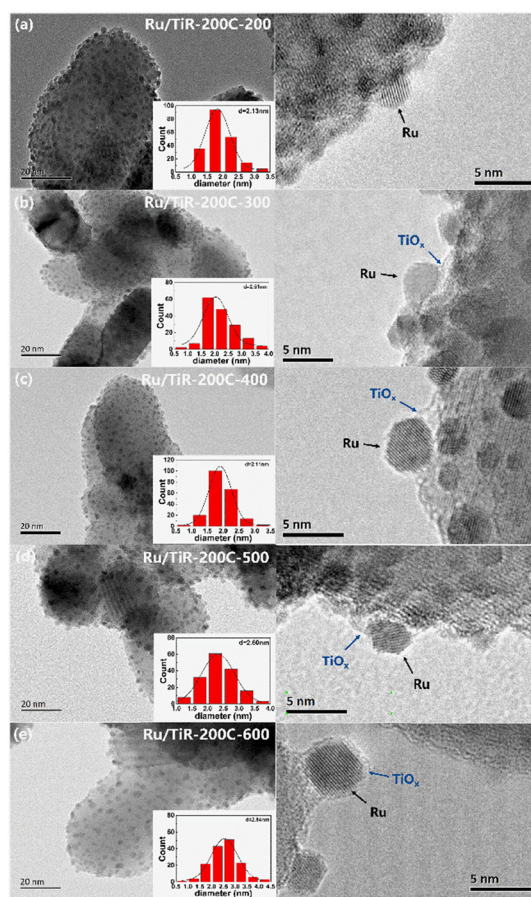


Fig. 9 TEM images of (a) Ru/TiR-200C-200, (b) Ru/TiR-200C-300, (c) Ru/TiR-200C-400, (d) Ru/TiR-200C-500, and (e) Ru/TiR-200C-600 and the particle size distribution of each catalyst.



the XRD results (Fig. S4†). It is found that the microstructure of the rutile TiO<sub>2</sub> support and the Ru particle sizes are almost unchanged by the increased reduction temperature. However, it is notable that the discrepancies in the microstructures of Ru particles on the rutile TiO<sub>2</sub> support are significant when samples are reduced at different temperatures. In detail, a distinct edge of regular spherical Ru particles can be observed on the rutile TiO<sub>2</sub> support when the sample is reduced at 200 °C (Fig. 9(a)), while a visible overlayer on the Ru particles can be more distinguishable with the higher catalyst reduction temperature. The visible overlayer is ascribed to the TiO<sub>x</sub> overlayer covering the Ru particles under high-temperature reduction conditions, and the more TiO<sub>x</sub> overlayer covers the Ru particle surface by further increasing the reduction temperature (Fig. 9(b–d)). When the sample is reduced at 600 °C, the Ru particle surface is almost completely covered by the TiO<sub>x</sub> overlayer (Fig. 9(e)). The TEM images reveal that the Ru particles of the Ru/rutile catalysts are covered with a thin overlayer, indicating the potential formation of the SMSI, and the extent of coverage can be modulated by adjusting the catalyst reduction temperature.

In the case of reducible metal oxides like TiO<sub>2</sub>-supported noble metal catalyst systems, it is reported that support species migrate to the metal surface from the support when H<sub>2</sub> reductive pretreatment at elevated temperature (≥400 °C) induces the SMSI, which decreases the chemisorption amounts of H<sub>2</sub> or CO on metal particles.<sup>37,60</sup> Thus, the CO chemisorption measurements are carried out on the Ru/rutile catalysts reduced at different temperatures to confirm the formation of SMSI, and the results are listed in Table 2. The CO chemisorption amounts clearly decrease from 116.3 μmol g<sup>−1</sup> to 13.0 μmol g<sup>−1</sup> with the catalyst reduction temperature increasing from 200 °C to 600 °C. The significant decrease of CO chemisorption amounts suggests that the number of CO adsorption sites in Ru particles reduces, which can be explained by the increase of the Ru particle sizes or the coverage of support species on Ru particles. However, according to the TEM images, the Ru particle size of each catalyst is similar (~3 nm). It suggests that the changes in CO chemisorption amounts are not caused by the changes in

the Ru particle sizes. Combined with the results of TEM images, the surface of Ru particles has a large amount of TiO<sub>x</sub> overlayer, which blocks the chemisorption of CO on Ru particles. Almost no CO can be chemically adsorbed on the Ru/TiR-200C-600 catalyst, implying the almost full coverage of the Ru particles by the TiO<sub>x</sub> overlayer. The above results are in good agreement with the TEM observations and confirm the formation of SMSI.

As shown in Fig. 10, the exposed surface atomic states of Ru nanoparticles were characterized by using *in situ* CO-DRIFTS spectra at room temperature to investigate the different MSI states on the Ru/rutile catalysts reduced at different temperatures. The CO spectrum of the Ru/TiR-200C-200 catalyst has four distinct bands at 2140, 2076, 2045, and 2012 cm<sup>−1</sup> in the carbonyl region. Specifically, the bands at 2140 and 2076 cm<sup>−1</sup> are ascribed to the symmetric and asymmetric stretches of bicarbonyl species that adsorbed on the uncoordinated Ru sites.<sup>62,63</sup> The band at 2045 cm<sup>−1</sup> is assigned to linear CO adsorption on small Ru clusters, and the weak band at 2012 cm<sup>−1</sup> is related to CO adsorption on slightly larger Ru particles.<sup>64–66</sup> Both the total band intensities and the positions of CO adsorbed on the catalyst surface for the Ru/rutile catalysts reduced at different temperatures are significantly different. In detail, the four CO band intensities of each CO spectrum gradually decrease with the reduction temperature increasing. In particular, the CO band adsorption on the Ru/TiR-200C-600 catalyst decreased by ~90% in intensity in comparison with that on the Ru/TiR-200C-200 catalyst, which suggests the significant loss of CO adsorption capacity observed for the Ru/TiR-200C-600 catalyst. The result of CO chemisorption measurements (Table 2) is consistent with this trend of the above phenomenon. The decreased band intensities mean decreased CO adsorption amounts. Given the similar Ru particle sizes over the Ru/rutile catalysts reduced at different temperatures (Fig. 9), this decrease in CO adsorption ability is attributed to the characteristic of SMSI formation.<sup>67</sup> In addition, the four CO bands of each spectrum shift slightly to lower wavenumbers with the reduction temperature increasing. The red shift of these bands is caused by the

**Table 2** The chemical properties of Ru/rutile catalysts reduced at different temperatures

Catalysts	$d_{\text{Ru}}^a$ nm	CO uptake μmol g <sup>−1</sup>	$d'_{\text{Ru}}^b$ nm	$D^c$ %	$\theta_Y^d$ %	$\eta^e$ %	$P^f$ nm	Acid amount <sup>g</sup> mmol g <sup>−1</sup>
Ru/TiR-200C-200	2.13	116.3	4.6	59.2	0	59.2	0	0.309
Ru/TiR-200C-300	2.51	106.0	5.0	51.4	8.9	46.8	4.5	0.236
Ru/TiR-200C-400	2.11	63.8	7.8	61.1	45.1	33.5	6.6	0.220
Ru/TiR-200C-500	2.60	58.1	9.2	49.6	50.1	24.8	8.2	0.162
Ru/TiR-200C-600	2.84	13.0	38.3	45.4	88.8	5.1	5.6	0.124

<sup>a</sup> Ru particle size is calculated by the TEM images according to  $d = \sum n_i d_i^3 / \sum n_i d_i^2$ . <sup>b</sup> Ru particle size is calculated by the CO chemisorption. <sup>c</sup>  $D = 1.29/d_{\text{Ru}}$ ,<sup>61</sup> where  $D$  is the dispersion of Ru particles and  $d_{\text{Ru}}$  is the average size of Ru particles over Ru/rutile catalysts. <sup>d</sup>  $\theta_Y = (Q_{200} - Q_Y)/Q_{200} \times 100\%$ , where  $\theta_Y$  is the coverage of TiO<sub>x</sub> to Ru particles over Ru/rutile catalysts reduced at  $Y$  °C,  $Q_{200}$  is the CO chemisorption amount over Ru/rutile catalysts reduced at 200 °C and  $Q_Y$  is the CO chemisorption amount over Ru/rutile catalysts reduced at  $Y$  °C. <sup>e</sup>  $\eta = D(1 - \theta_Y)$ ,  $\eta$  is the fraction of Ru atoms that are exposed on the Ru particles' surface after Ru particles have been covered by the TiO<sub>x</sub> overlayer.

<sup>f</sup>  $P = 2\pi d \sqrt{(\theta_Y - \theta_Y^2)}$ ,  $P$  is the interface perimeter between Ru and TiO<sub>x</sub> over Ru/rutile catalysts with different reduction temperatures. <sup>g</sup> Acid amount calculated by NH<sub>3</sub>-TPD.

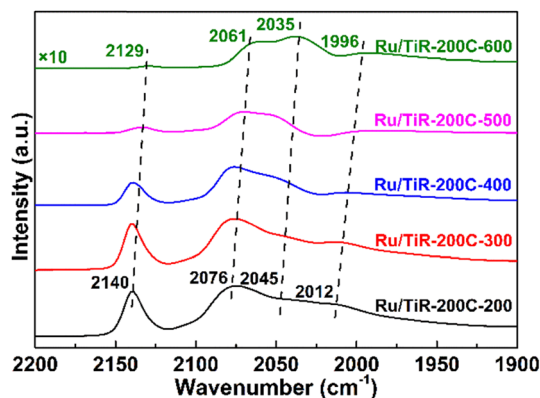


Fig. 10 *In situ* CO-DRIFTS of Ru/TiO<sub>2</sub> catalysts with different reduction temperatures.

dipole–dipole coupling effect of the adsorbed CO species with the number of CO molecules decreasing.<sup>63,68</sup>

Besides the changes in the total band intensities and positions, the relative intensities of the bands also change, notably, the stronger relative intensity of the CO band adsorption on small Ru clusters and the weaker relative intensity of the CO band adsorption on the uncoordinated Ru sites of Ru particles' edge in the same CO spectrum with the reduction temperature increasing. These changes mean that the ratios of uncoordinated Ru sites decrease after high-temperature reduction. In general, the ratio of low coordinated surface atoms decreases with increased metal nanoparticle sizes. However, the Ru particle sizes over the Ru/rutile catalysts reduced at different temperatures are 2.1–2.8 nm (Fig. 9), which are almost the same. This suggests that the relatively weaker band intensities are not attributed to the increased particle sizes but are caused by the coverage of the TiO<sub>x</sub> overlayer. As the catalyst reduction temperature increases from 200 °C to 600 °C, it is constantly aggravated so that the surface of Ru particles on the Ru/rutile catalysts is covered by the TiO<sub>x</sub> overlayer formed through SMSI. The TiO<sub>x</sub> overlayer gradually covers the unsaturated Ru sites on the Ru particle surface, leading to a decline in the CO chemical adsorption amount and a more obvious CO dipole–dipole coupling effect. This causes a decrease in the total CO band intensities, a change in the relative band intensities, and a redshift of the band positions. The CO-DRIFTS spectra also confirm that the catalyst reduction temperature governs the coverage extent of the TiO<sub>x</sub> overlayer formed by SMSI on the Ru particles' surface over the Ru/rutile catalysts.

The chemical states of the Ru/rutile catalysts calcined at 200 °C and reduced at different temperatures are investigated using XPS. Fig. 11(a) shows the Ru 3d XPS fitting results over the Ru/rutile catalysts. The spectra of the Ru 3d<sub>5/2</sub> peak of the Ru/TiR-200C-200 catalyst are fitted in two parts located at ~280.3 eV and ~281.3 eV, which are ascribed to metallic Ru<sup>0</sup> and oxidized Ru<sup>X+</sup> species (0 < X < 4) at the Ru–TiO<sub>x</sub> interfaces, respectively. With the reduction temperature increasing from 200 °C to 600 °C, the binding energies of Ru species do not exhibit significant changes in temperature.

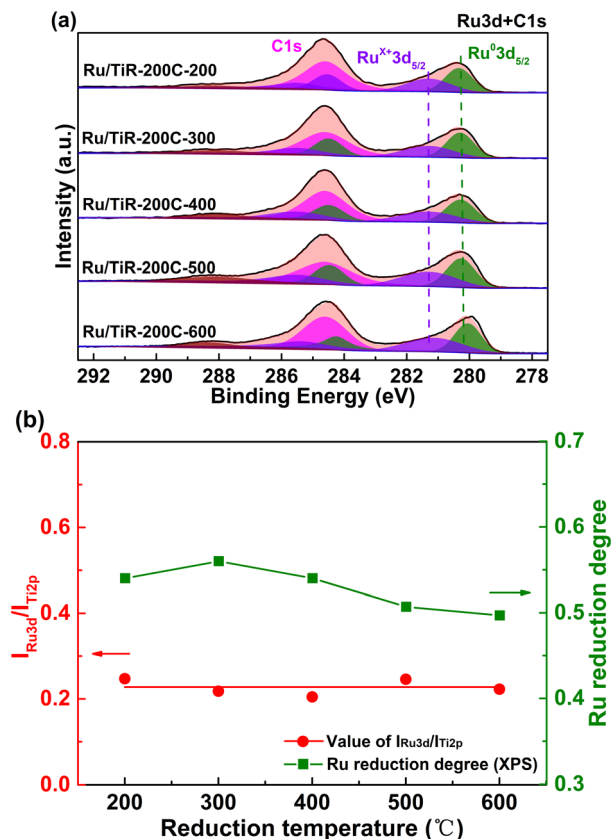


Fig. 11 (a) The XPS fitting results of Ru 3d and (b) the values of  $I_{\text{Ru}3\text{d}}/I_{\text{Ti}2\text{p}}$  (based on the XPS peak area ratios of Ru 3d and Ti 2p) and Ru reduction degrees (Ru reduction degree (XPS) is calculated based on XPS peak fitting area ratios of Ru<sup>0</sup> and Ru<sup>X+</sup>) with different reduction temperatures over Ru/rutile catalysts.

Fig. 11(b) shows the influence of catalyst reduction temperature on the relative content value of  $I_{\text{Ru}3\text{d}}/I_{\text{Ti}2\text{p}}$  (calculated quantitatively with the XPS peak area ratio of Ru 3d and Ti 2p) and Ru reduction degree (calculated quantitatively with the XPS peak area ratio of Ru<sup>0</sup> and Ru<sup>X+</sup>) over the Ru/rutile catalysts. The  $I_{\text{Ru}3\text{d}}/I_{\text{Ti}2\text{p}}$  values (Table S2†) of the Ru/rutile catalysts almost remain constant (~0.23) as the reduction temperature increases, which suggests that the concentration of Ru species on each catalyst is similar. This phenomenon is attributed to the highly uniform distribution of Ru particles on each catalyst surface with similar particle sizes (~3 nm). The above results are consistent with the observation results of TEM images (Fig. 9). In addition, Ru reduction degrees are significantly decreased from 0.540 to 0.497 with the reduction temperature increasing from 200 °C to 600 °C (Table S2†), suggesting that the relative contents of Ru<sup>X+</sup> species increased. Considering the same Ru loadings (~4 wt%) and similar Ru particle sizes (~3 nm) in the Ru/rutile catalysts, the increased Ru<sup>X+</sup> species can be ascribed to more Ru–TiO<sub>x</sub> interfaces formed by the TiO<sub>x</sub> overlayer coating the Ru particle surface. The above results suggest that the Ru/rutile catalysts have more interfaces between the Ru particles and the rutile TiO<sub>2</sub> support with the higher catalyst reduction temperature.

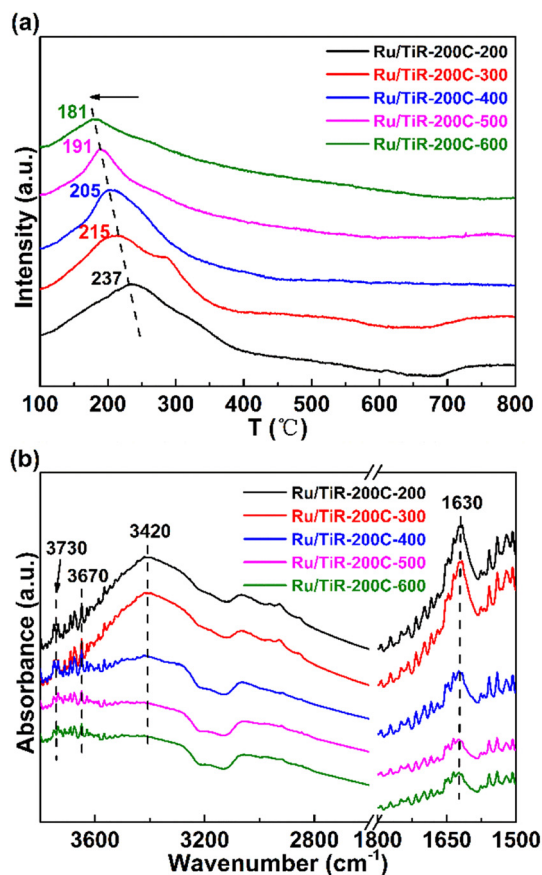


Fig. 12 (a) NH<sub>3</sub>-TPD profiles and (b) hydroxyl group IR spectra of Ru/rutile catalysts with different reduction temperatures.

NH<sub>3</sub>-TPD is employed to gain information on the intensity and amount of the surface acidity in the Ru/rutile catalysts with different reduction temperatures. Fig. 12(a) shows the results of NH<sub>3</sub>-TPD profiles and the NH<sub>3</sub> desorption amounts are listed in Table 2. Each NH<sub>3</sub>-TPD profile exhibits a single NH<sub>3</sub> desorption peak at a temperature range of 150–300 °C, assigned to the weak surface acid sites. With the reduction temperature increasing, the peak intensities decline and the peak positions shift to the lower temperature (237 °C → 181 °C). As shown in Table 2, the surface acidity amounts of catalysts significantly decrease from 0.309 mmol g<sup>-1</sup> to 0.124 mmol g<sup>-1</sup> with the reduction temperature increasing. A lower desorption temperature corresponds to a weaker acidity. The above results indicate that the higher catalyst reduction temperature decreases the acid strength and acid sites of the Ru/rutile catalysts.

Fig. 12(b) shows the hydroxyl group IR spectra of the Ru/rutile catalysts reduced at different temperatures. In detail, the two small shoulder bands at 3730 and 3670 cm<sup>-1</sup> are related to the terminally bound hydroxyl groups and isolated bridge bonded hydroxyl groups,<sup>69,70</sup> respectively. A broad band between 3300 and 3600 cm<sup>-1</sup> is attributed to the stretching mode of hydrogen-bonded hydroxyl groups and a sharp band at 1630 cm<sup>-1</sup> belongs to the bending mode of

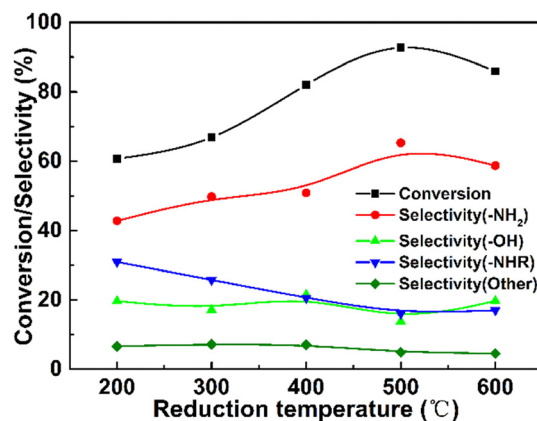


Fig. 13 The catalytic hydrogenation performance of butyramide over Ru/TiR-200C-Y catalysts. Reaction conditions: 300 mg catalyst, 3 mmol butyramides, 25 mL CPME, 150 °C, 5 MPa H<sub>2</sub>, and 4 h.

intact H<sub>2</sub>O.<sup>71</sup> These bands are decreased in intensity when the catalyst reduction temperature increases from 200 °C to 600 °C, meaning that the amount of surface hydroxyl groups decreases. This trend is consistent with the results of NH<sub>3</sub>-TPD. Therefore, the change in acidity could be explained by the reduced amount of surface hydroxyl groups in the Ru/rutile catalysts at different temperatures.

**3.3.2 The catalytic amide hydrogenation performance of Ru/rutile catalysts reduced at different temperatures.** Fig. 13 shows the catalytic performance for the butyramide hydrogenation over the Ru/rutile catalysts with different reduction temperatures. For the Ru/TiR-200C-200 catalyst, the conversion of butyramide is 61%, and selectivity to butylamine, 1-butanol, dibutylamine, and *N*-butylbutanamide is 43%, 19%, 31%, and 7%, respectively, over the catalyst calcined at 200 °C. With the higher catalyst reduction temperature, the catalytic performance is improved significantly. The Ru/TiR-200C-500 catalyst exhibited the best catalytic activity among all the catalysts, with 93% conversion, 65% selectivity to butylamine, 14% selectivity to 1-butanol, 16% selectivity to dibutylamine and 5% selectivity to *N*-butylbutanamide. However, for the Ru/TiR-200C-600 catalyst, the catalytic performance slightly decreased, with 86% conversion, 59% selectivity to butylamine, 19% selectivity to 1-butanol, 17% selectivity to dibutylamine and 5% selectivity to *N*-butylbutanamide. The butyramide conversion and selectivity to butylamine vary with the catalyst reduction temperature increasing from 200 °C to 600 °C in a volcano-type relationship, while selectivity to 1-butanol and *N*-butylbutanamide remains nearly invariant. It is also noted that the selectivity to dibutylamine decreased from 31% to 16% monotonously. The changes of selectivity to butylamine and dibutylamine mean the suppression of butylamine and imine intermediate condensation to dibutylamine (Scheme 1).<sup>72–74</sup> The change in butyramide conversion means the change in the number of active sites for amide hydrogenation over the Ru/rutile catalysts, suggesting that the active sites can be influenced by the catalyst reduction temperature.



### 3.4 Understanding of the structure–performance relationship

Kinetic experiments were conducted over the Ru/rutile catalysts with different reduction temperatures to explore their intrinsic behaviors in butyramide hydrogenation reactions. The reaction orders of butyramide and H<sub>2</sub> are evaluated by plotting the logarithm of the reaction rate *versus* the logarithm of butyramide concentration and H<sub>2</sub> pressure. The reaction rates were calculated from the converted amount of butyramide divided by the reaction time and the catalyst amount at low conversion (<35%) of butyramide (Table S3 and Fig. S5†). Table 3 shows the reaction orders of butyramide over the Ru/rutile catalysts reduced at different temperatures. The reaction orders with respect to the butyramide concentration over the Ru/rutile catalysts are calculated to decrease from 0.5 to −0.1 with the catalyst reduction temperature increasing from 200 °C to 600 °C. These results mean that butyramide is more strongly adsorbed on the Ru/rutile catalysts with the catalyst reduction temperature increasing, suggesting a greater number of active sites for butyramide with higher catalyst reduction temperature. The close to zero reaction order of butyramide suggests that the butyramide is saturated on the catalyst surface. Table 3 also shows the reaction orders of H<sub>2</sub> over the Ru/rutile catalysts reduced at different temperatures. The reaction orders with respect to the H<sub>2</sub> pressure over the Ru/rutile catalysts are calculated to decrease from 1.6 to 0.5 with the reduction temperature increasing from 200 °C to 600 °C. The decreased reaction order suggests that H<sub>2</sub> is more strongly adsorbed on the catalyst surface. The positive reaction order indicates that the reaction rate is strongly influenced by the H<sub>2</sub> pressure. On the other hand, it is noted that the reaction orders of H<sub>2</sub> are greater than that of butyramide over the Ru/rutile catalysts reduced at different temperatures. It suggests that the rate-determining step of the butyramide hydrogenation reaction might depend more on the adsorption and activation of H<sub>2</sub> and not butyramide.

Although the Ru particle sizes are similar over the Ru/rutile catalysts reduced at different temperatures, the catalytic performance of amide hydrogenation is significantly different over these catalysts. Considering that partially reduced TiO<sub>x</sub> species cover Ru particles to varying degrees due to SMSI over Ru catalysts after high-temperature H<sub>2</sub> reduction treatments, differences in the number of Ru atoms exposed and the Ru–TiO<sub>x</sub> boundary are expected. Combined with the results of TEM images (Fig. 9) and CO

chemisorption (Table 2), we established a Ru/rutile catalyst model in which the Ru particle was covered by a TiO<sub>x</sub> overlayer (assuming an ideal spheroidal Ru particle on rutile TiO<sub>2</sub>) (Fig. 14(a and b)). Assuming that the Ru–TiO<sub>x</sub> boundary is an ideal round shape, the boundary perimeter values of the Ru/TiO<sub>2</sub> catalysts are calculated in Table 2 and the detailed deduction of the formula is shown in the ESI† (Fig. S6). Ru particles on the rutile TiO<sub>2</sub> are hardly modified by TiO<sub>x</sub> species at a reduction temperature of 200 °C. The coverage of TiO<sub>x</sub> species on Ru particles is defined as 0 and the formed Ru–TiO<sub>x</sub> boundary perimeter is also set to 0. As the catalyst reduction temperature increases, the Ru particle surface is gradually covered by more TiO<sub>x</sub> overlayer and thus generates a more abundant Ru–TiO<sub>x</sub> boundary, resulting in fewer Ru atoms exposed on Ru particles (Fig. 14(c)). When the catalyst is reduced at 500 °C, the coverage of the TiO<sub>x</sub> overlayer on Ru particles reaches 50.1% and the Ru–TiO<sub>x</sub> boundary perimeter reaches the maximum length value (8.2 nm). When the reduction temperature continues to increase to 600 °C, the TiO<sub>x</sub> overlayer almost completely covers the Ru particle surface, leading to the Ru–TiO<sub>x</sub> boundary perimeter decreasing (5.6 nm).

Therefore, the fraction of Ru atoms exposed ( $\eta$ ) and the boundary perimeter ( $P$ ) between Ru and TiO<sub>x</sub> species are calculated by using Ru dispersity and TiO<sub>x</sub> coverage, respectively, which are both listed in Table 2. As the catalyst reduction temperature increases from 200 °C to 600 °C, the  $\eta$  value gradually decreases from 59.2% to 5.1% over the Ru/rutile catalysts. Apparently, the monotonously decreasing trend of the  $\eta$  value is inconsistent with the change of butyramide conversion, proving that exposed Ru atoms are not the active sites of the amide hydrogenation reaction. However, the  $P$  value exhibits a volcano-type relationship with catalyst reduction temperatures, which positively follows the same trend as the butyramide conversion in Fig. 14(d). When the catalyst reduction temperature reaches 500 °C, the catalyst achieves the highest butyramide conversion and has the maximum Ru–TiO<sub>x</sub> boundary perimeter. The high correlation between the Ru–TiO<sub>x</sub> boundary perimeter and the catalytic activity of the butyramide hydrogenation over the Ru/rutile catalysts demonstrates that the Ru–TiO<sub>x</sub> boundary is responsible for the conversion of amide. Thus, the  $P$  value can be used as the descriptor to indicate the number of active sites over the Ru/rutile catalysts.

In addition, it is also noted that the selectivity to dibutylamine decreases monotonously with the reduction temperature increasing over the Ru/rutile catalysts (Fig. 13). Through the analysis of NH<sub>3</sub>-TPD and hydroxyl group IR spectra (Fig. 12) of Ru/rutile catalysts reduced at different temperatures, a significant positive correlation is observed between the quantity of hydroxyl groups on the catalyst surface and the amount of NH<sub>3</sub> desorbed. This finding indicates that the catalyst acidity predominantly might originate from its surface hydroxyl groups. Furthermore, a strong positive correlation is also identified between catalyst acid amounts and the selectivity to dibutylamine (Fig. 15). It

**Table 3** The kinetic parameters over the Ru/TiO<sub>2</sub> catalysts with different reduction temperatures

Catalysts	Reaction orders	
	Butyramide	H <sub>2</sub>
Ru/TiR-200C-200	0.5	1.6
Ru/TiR-200C-300	0.1	1.0
Ru/TiR-200C-400	−0.1	0.5
Ru/TiR-200C-500	0.1	0.6
Ru/TiR-200C-600	−0.1	0.5

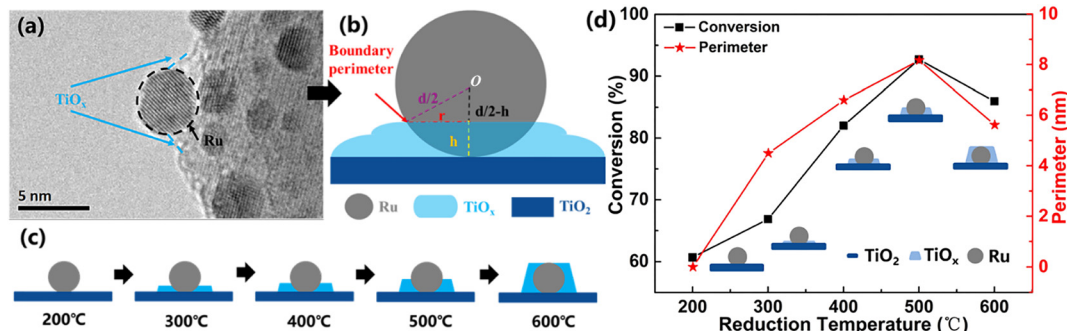


Fig. 14 (a) The observed structure of the Ru/rutile catalyst, (b) the proposed structural model of the Ru/rutile catalyst, (c) the schematic illustration of the structural evolution of Ru/rutile catalysts at different reduction temperatures, and (d) the relationship of the butyramide conversion with the Ru-TiO<sub>x</sub> boundary perimeter over Ru/rutile catalysts reduced at different temperatures.

was reported that the hydroxyl groups of the catalyst surface and/or solvent, such as water and alcohol, are considered to have adverse effects on the amide hydrogenation process. Nakagawa *et al.* reported that the addition of CeO<sub>2</sub> to Rh-Mo/SiO<sub>2</sub> catalyst sufficiently decreased the number of hydroxyl groups on the catalyst surface and increased the active site interaction with the amide, improving the amide conversion.<sup>9</sup> Beamson and Coeck *et al.* proposed that the terrible catalytic hydrogenation performance of amide observed in solvents containing hydroxyl groups was attributed to the strong interaction between the amide group and the hydroxyl functional group of the solvent.<sup>5,12</sup> These results suggest that the number of hydroxyl groups and adsorbed water molecules on the catalyst surface decreases with the catalyst reduction temperature increasing, leading to a reduction in the surface acid amount of the catalyst. The catalyst surface acidity can affect the adsorption/desorption of butylamines and imine intermediates, and the low acidity of the catalyst surface is beneficial for the timely desorption of butylamines and imine intermediates from the catalyst surface, thereby suppressing the condensation reactions of the imine intermediates with butylamines, reducing the consumption of butylamine, and improving the selectivity to butylamine. Overall, the formation of dibutylamine is inhibited and the

selectivity to butylamine is enhanced because of the low acidity of the catalyst surface.

To summarize, we showed that the catalytic amide hydrogenation performance of Ru/rutile catalysts depends on the boundary between the Ru particles and the rutile TiO<sub>2</sub> support. This feature is induced by the SMSI during the high-temperature reduction. As the catalyst reduction temperature increases, more TiO<sub>x</sub> overlayers migrate to the Ru particle surface and form a more abundant Ru-TiO<sub>x</sub> boundary, which is responsible for the activation of amide. The active H species adsorbed on Ru particles overflow onto the activated amide in the Ru-TiO<sub>x</sub> boundary. Furthermore, high-temperature reduction also reduces the surface acidity of catalysts and consequently suppresses secondary side reactions. However, when Ru particles are almost completely covered by TiO<sub>x</sub> at a higher reduction temperature, the Ru-TiO<sub>x</sub> boundary is decreased, which is not conducive to the amide catalytic hydrogenation reaction.

## 4. Conclusions

In summary, we investigated the enhancement effect of TiO<sub>2</sub> crystal phases, calcination, and reduction temperatures on the Ru/TiO<sub>2</sub> catalysts in the hydrogenation of butyramide. Our study shows that rutile TiO<sub>2</sub> plays an important role in preventing agglomeration of Ru particles under high-temperature calcination conditions because of the lattice match between rutile TiO<sub>2</sub> and RuO<sub>2</sub>. The catalyst calcination temperature adjusted the Ru particle sizes on rutile TiO<sub>2</sub>, and small Ru particles favor the amide hydrogenation reaction. By optimizing the reduction temperature of the Ru/rutile catalysts, the Ru/TiR-200C-500 catalyst (reduced at 500 °C) presented the most outstanding catalytic amide hydrogenation performance at 150 °C with 5 MPa H<sub>2</sub> and achieved 93% butyramide conversion and 65% selectivity to butylamine. Due to SMSI, the Ru particles are covered by a TiO<sub>x</sub> overlayer and form an abundant Ru-TiO<sub>x</sub> boundary. The Ru-TiO<sub>x</sub> boundary provides the greatest number of active sites over the Ru/rutile catalyst reduced at 500 °C for high butyramide conversion. Furthermore, Ru/rutile catalysts reduced at higher temperatures also inhibit

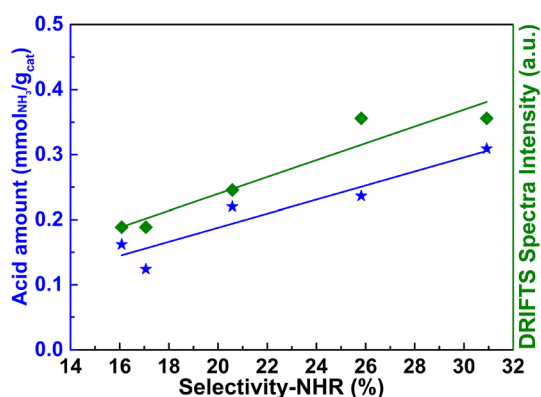


Fig. 15 The relationship of the dibutylamine selectivity with the acid amounts and the number of surface hydroxyl groups over Ru/rutile catalysts reduced at different temperatures.

the formation of dibutylamine because of the decrease in surface acidity. This study strengthens the understanding of the effect of SMSI on Ru/rutile catalysts and provides new insight into designing highly efficient catalysts for the amide hydrogenation reactions by optimizing the interaction between metal and support.

## Data availability

The data supporting this article have been included as part of the ESI.†

## Conflicts of interest

There are no conflicts to declare.

## Notes and references

- 1 A. M. Smith and R. Whyman, *Chem. Rev.*, 2014, **114**, 5477–5510.
- 2 J. R. Cabrero-Antonino, R. Adam, V. Papa and M. Beller, *Nat. Commun.*, 2020, **11**, 3893.
- 3 C. Hirose, N. Wakasa and T. Fuchikami, *Tetrahedron Lett.*, 1996, **37**, 6749–6752.
- 4 G. Beamson, A. J. Papworth, C. Philipps, A. M. Smith and R. Whyman, *J. Catal.*, 2010, **269**, 93–102.
- 5 G. Beamson, A. J. Papworth, C. Philipps, A. M. Smith and R. Whyman, *Adv. Synth. Catal.*, 2010, **352**, 869–883.
- 6 G. Beamson, A. J. Papworth, C. Philipps, A. M. Smith and R. Whyman, *J. Catal.*, 2011, **278**, 228–238.
- 7 M. Stein and B. Breit, *Angew. Chem., Int. Ed.*, 2013, **52**, 2231–2234.
- 8 R. Burch, C. Paun, X. Cao, P. Crawford, P. Goodrich, C. Hardacre, P. Hu, L. McLaughlin, J. Sa and J. M. Thompson, *J. Catal.*, 2011, **283**, 89–97.
- 9 Y. Nakagawa, R. Tamura, M. Tamura and K. Tomishige, *Sci. Technol. Adv. Mater.*, 2015, **16**, 014901.
- 10 T. Mitsudome, K. Miyagawa, Z. Maeno, T. Mizugaki, K. Jitsukawa, J. Yamasaki, Y. Kitagawa and K. Kaneda, *Angew. Chem., Int. Ed.*, 2017, **56**, 9381–9385.
- 11 T. Chen, Z. Shi, G. Zhang, H. C. Chan, Y. J. Shu, Q. S. Gao and Y. Tang, *ACS Appl. Mater. Interfaces*, 2018, **10**, 42475–42483.
- 12 R. Coeck, S. Berden and D. E. De Vos, *Green Chem.*, 2019, **21**, 5326–5335.
- 13 A. Penner, W. Y. Hernandez, B. T. Kusema and S. Streiff, *Appl. Catal., A*, 2021, **624**, 118301.
- 14 Y. Zhang, L. Li, F. Liu, H. Qi, L. Zhang, W. Guan, Y. Liu, A. Wang and T. Zhang, *ACS Catal.*, 2022, **12**, 6302–6312.
- 15 Y. Zhang, F. Zhang, L. Li, H. F. Qi, Z. A. Yu, X. Y. Liu, C. Cao, F. Liu, A. Q. Wang and T. Zhang, *J. Catal.*, 2023, **417**, 301–313.
- 16 Y. Zhang, F. Zhang, L. Li, F. Liu and A. Q. Wang, *ChemistrySelect*, 2022, **7**, e202203030.
- 17 R. Y. Qu, S. X. Mao, J. Weiss, V. A. Kondratenko, E. V. Kondratenko, S. Bartling, H. F. Qi, A. E. Surkus, K. Junge and M. Beller, *Catal. Sci. Technol.*, 2024, **14**, 90–97.
- 18 K. Shimizu, W. Onodera, A. S. Touchy, S. M. A. H. Siddiki, T. Toyao and K. Kon, *ChemistrySelect*, 2016, **1**, 736–740.
- 19 T. Toyao, S. M. A. H. Siddiki, Y. Morita, T. Kamachi, A. S. Touchy, W. Onodera, K. Kon, S. Furukawa, H. Ariga, K. Asakura, K. Yoshizawa and K. Shimizu, *Chem. – Eur. J.*, 2017, **23**, 14848–14859.
- 20 W. J. Guo, Q. N. Xia, H. Y. Jia, Y. Guo, X. H. Liu, H. Pan, Y. G. Wang and Y. Q. Wang, *Chem. – Asian J.*, 2022, **17**, e202101256.
- 21 J. Y. Fu, J. Lym, W. Q. Zheng, K. Alexopoulos, A. V. Mironenko, N. Li, J. A. Boscoboinik, D. Su, R. T. Weber and D. G. Vlachos, *Nat. Catal.*, 2020, **3**, 446–453.
- 22 S. N. Ding and X. L. Zhu, *ChemCatChem*, 2024, **16**, e202301552.
- 23 H. Li, S. J. Zha, Z. J. Zhao, H. Tian, S. Chen, Z. M. Gong, W. T. Cai, Y. N. Wang, Y. Cui, L. Zeng, R. T. Mu and J. L. Gong, *ACS Catal.*, 2018, **8**, 5526–5532.
- 24 N. Aranda-Perez, M. P. Ruiz, J. Echave and J. Faria, *Appl. Catal., A*, 2017, **531**, 106–118.
- 25 J. J. Tan, J. L. Cui, X. J. Cui, T. S. Deng, X. Q. Li, Y. L. Zhu and Y. W. Li, *ACS Catal.*, 2015, **5**, 7379–7384.
- 26 K. L. Zhang, Q. L. Meng, H. H. Wu, T. Y. Yuan, S. T. Han, J. X. Zhai, B. X. Zheng, C. Y. Xu, W. Wu, M. Y. He and B. X. Han, *Green Chem.*, 2021, **23**, 1621–1627.
- 27 H. R. Yang, H. Garcia and C. W. Hu, *Green Chem.*, 2024, **26**, 2341.
- 28 C. Hernandez-Mejia, E. S. Gnanakumar, A. Olivos-Suarez, J. Gascon, H. F. Greer, W. Z. Zhou, G. Rothenberg and N. R. Shiju, *Catal. Sci. Technol.*, 2016, **6**, 577–582.
- 29 X. Li, J. Lin, L. Li, Y. Huang, X. Pan, S. E. Collins, Y. Ren, Y. Su, L. Kang, X. Liu, Y. Zhou, H. Wang, A. Wang, B. Qiao, X. Wang and T. Zhang, *Angew. Chem., Int. Ed.*, 2020, **59**, 19983–19989.
- 30 T. Omotoso, S. Boonyasuwan and S. P. Crossley, *Green Chem.*, 2014, **16**, 645–652.
- 31 J. Zhang, L. Pei, J. Wang, P. Zhu, X. Gu and Z. Zheng, *Catal. Sci. Technol.*, 2020, **10**, 1518–1528.
- 32 A. P. Jia, W. Zhang, H. T. Peng, Y. S. Zhang, T. Y. Song, L. Li, Y. W. Ye, Y. Wang, M. F. Luo, D. L. Chen, W. X. Huang and J. Q. Lu, *J. Catal.*, 2023, **425**, 57–69.
- 33 F. C. Meng, X. C. Yang, S. C. Zhao, Z. Li, G. K. Zhang, Y. T. Qi, S. Q. Chu, G. F. Wang, J. Zhang, Y. Qin and B. Zhang, *Appl. Catal., B*, 2023, **324**, 122236.
- 34 Z. J. Zhong, J. X. Li, M. Y. Jian, R. Y. Shu, Z. P. Tian, C. Wang, Y. Chen, N. Shi and Y. X. Wu, *Fuel*, 2023, **333**, 126241.
- 35 J. H. Xu, X. Su, H. M. Duan, B. L. Hou, Q. Q. Lin, X. Y. Liu, X. L. Pan, G. X. Pei, H. R. Geng, Y. Q. Huang and T. Zhang, *J. Catal.*, 2016, **333**, 227–237.
- 36 W. L. Tu, M. Y. Chu, X. P. Wang, X. C. Wang, Y. F. Li, W. X. Yang, M. H. Cao, L. Wang, Y. Y. Li, T. K. Sham, Y. Cui, Q. Zhang and J. X. Chen, *Appl. Catal., B*, 2023, **339**, 123122.
- 37 Y. R. Zhang, W. J. Yan, H. F. Qi, X. Su, Y. Su, X. Y. Liu, L. Li, X. F. Yang, Y. Q. Huang and T. Zhang, *ACS Catal.*, 2022, **12**, 1697–1705.
- 38 T. W. van Deelen, C. H. Mejia and K. P. de Jong, *Nat. Catal.*, 2019, **2**, 955–970.



- 39 M. Xu, M. Peng, H. L. Tang, W. Zhou, B. T. Qiao and D. Ma, *J. Am. Chem. Soc.*, 2024, **146**, 2290–2307.
- 40 A. Kim, D. P. Debecker, F. Devred, V. Dubois, C. Sanchez and C. Sassoie, *Appl. Catal., B*, 2018, **220**, 615–625.
- 41 J. L. G. de la Fuente, M. V. Martínez-Huerta, S. Rojas, P. Hernández-Fernández, P. Terreros, J. L. G. Fierro and M. A. Peña, *Appl. Catal., B*, 2009, **88**, 505–514.
- 42 A. Kim, C. Sanchez, G. Patriarche, O. Ersen, S. Moldovan, A. Wisnet, C. Sassoie and D. P. Debecker, *Catal. Sci. Technol.*, 2016, **6**, 8117–8128.
- 43 L. M. Martínez, T. A. Muñoz, A. Pérez, O. H. Laguna, L. F. Bobadilla, M. A. Centeno and J. A. Odriozola, *Appl. Catal., A*, 2022, **641**, 118678.
- 44 D. X. Wang, J. Huang, F. Liu, X. L. Xu, X. Z. Fang, J. J. Liu, Y. C. Xie and X. Wang, *Catal. Today*, 2020, **339**, 220–232.
- 45 J. Zhou, Z. Gao, G. Xiang, T. Zhai, Z. Liu, W. Zhao, X. Liang and L. Wang, *Nat. Commun.*, 2022, **13**, 327.
- 46 Q. Pei, T. He, Y. Yu, Z. J. Jing, J. P. Guo, L. Liu, Z. T. Xiong and P. Chen, *ACS Appl. Mater. Interfaces*, 2020, **12**, 7071–7080.
- 47 R. D. Shannon, *Acta Crystallogr., Sect. A*, 1976, **32**, 751–767.
- 48 H. Ali, T. Vandevyvere, J. Lauwaert, S. K. Kansal, S. Saravanamurugan and J. W. Thybaut, *Catal. Commun.*, 2022, **164**, 106436.
- 49 R. Kumar and M. Kar, *Ceram. Int.*, 2016, **42**, 6640–6647.
- 50 J. Zhao, W. J. Xi, C. S. Tu, Q. G. Dai and X. Y. Wang, *Appl. Catal., B*, 2020, **263**, 118237.
- 51 L. Li, L. Qu, J. Cheng, J. Li and Z. Hao, *Appl. Catal., B*, 2009, **88**, 224–231.
- 52 D. Li, N. Ichikuni, S. Shimazu and T. Uematsu, *Appl. Catal., A*, 1999, **180**, 227–235.
- 53 H. Kim, J. H. Park, J.-M. Ha and D. H. Kim, *ACS Catal.*, 2023, 11857–11870.
- 54 Y. R. Zhang, X. Su, L. Li, H. F. Qi, C. Y. Yang, W. Liu, X. L. Pan, X. Y. Liu, X. F. Yang, Y. Q. Huang and T. Zhang, *ACS Catal.*, 2020, **10**, 12967–12975.
- 55 J. H. An, Y. H. Wang, J. M. Lu, J. Zhang, Z. X. Zhang, S. T. Xu, X. Y. Liu, T. Zhang, M. Gocyla, M. Heggen, R. E. Dunin-Borkowski, P. Fornasiero and F. Wang, *J. Am. Chem. Soc.*, 2018, **140**, 4172–4181.
- 56 R. Berthoud, P. Delichere, D. Gajan, W. Lukens, K. Pelzer, J. M. Basset, J. P. Candy and C. Coperet, *J. Catal.*, 2008, **260**, 387–391.
- 57 H. N. Aiyer, V. Vijayakrishnan, G. N. Subbanna and C. N. R. Rao, *Surf. Sci.*, 1994, **313**, 392–398.
- 58 S. C. Fung, *J. Catal.*, 1979, **58**, 454–469.
- 59 X. F. Yu, N. Z. Wu, H. Z. Huang, Y. C. Xie and Y. Q. Tang, *J. Mater. Chem.*, 2001, **11**, 3337–3342.
- 60 S. J. Tauster, S. C. Fung, R. T. K. Baker and J. A. Horsley, *Science*, 1981, **211**, 1121–1125.
- 61 Z. Y. Zhao, Q. R. Jiang, Q. X. Wang, M. Z. Wang, J. C. Zuo, H. M. Chen, Q. Kuang and Z. X. Xie, *ACS Sustainable Chem. Eng.*, 2021, **9**, 14288–14296.
- 62 A. M. Abdel-Mageed, K. Wiese, A. Hauble, J. Bansmann, J. Rabeah, M. Parlinska-Wojtan, A. Bruckner and R. J. Behm, *J. Catal.*, 2021, **401**, 160–173.
- 63 Y. Yan, Q. Wang, C. Jiang, Y. Yao, D. Lu, J. W. Zheng, Y. H. Dai, H. M. Wang and Y. H. Yang, *J. Catal.*, 2018, **367**, 194–205.
- 64 B. T. Loveless, C. Buda, M. Neurock and E. Iglesia, *J. Am. Chem. Soc.*, 2013, **135**, 6107–6121.
- 65 P. Panagiotopoulou, D. I. Kondarides and X. E. Verykios, *J. Phys. Chem. C*, 2011, **115**, 1220–1230.
- 66 A. M. Abdel-Mageed, D. Widmann, S. E. Olesen, I. Chorkendorff, J. Biskupek and R. J. Behm, *ACS Catal.*, 2015, **5**, 6753–6763.
- 67 F. Liu, J. Ftouni, P. C. A. Bruijninx and B. M. Weckhuysen, *ChemCatChem*, 2019, **11**, 2079–2088.
- 68 H. Pfnur, D. Menzel, F. M. Hoffmann, A. Ortega and A. M. Bradshaw, *Surf. Sci.*, 1980, **93**, 431–452.
- 69 J. C. Matsubu, S. Y. Zhang, L. DeRita, N. S. Marinkovic, J. G. G. Chen, G. W. Graham, X. Q. Pan and P. Christopher, *Nat. Chem.*, 2017, **9**, 120–127.
- 70 A. M. Abdel-Mageed, K. Wiese, M. Parlinska-Wojtan, J. Rabeah, A. Bruckner and R. J. Behm, *Appl. Catal., B*, 2020, **270**, 118846.
- 71 Y. Zhan, C. Zhou, F. Jin, C. Chen and L. Jiang, *Appl. Surf. Sci.*, 2020, **525**, 146627.
- 72 M. Degelin, S. Van Minnebruggen, R. Coeck and D. De Vos, *J. Catal.*, 2023, **428**, 115122.
- 73 C. Xie, J. L. Song, M. L. Hua, Y. Hu, X. Huang, H. R. Wu, G. Y. Yang and B. X. Han, *ACS Catal.*, 2020, **10**, 7763–7772.
- 74 T. Cuypers, T. Morias, S. Windels, C. Marquez, C. Van Goethem, I. Vankelecom and D. E. De Vos, *Green Chem.*, 2020, **22**, 1884–1893.